AGU PUBLICATIONS

JGR

Journal of Geophysical Research: Oceans

RESEARCH ARTICLE
10.1002/2015JC011273

Special Section:
Forum for Arctic Modeling and Observational Synthesis (FAMOS): Results and Synthesis of Coordinated Experiments

Accuracy of short-term sea ice drift forecasts using a coupled ice-ocean model

Axel J. Schweiger[1] and Jinlun Zhang[1]

[1]Polar Science Center, Applied Physics Laboratory, University of Washington, Seattle, Washington, USA

Key Points:
- Drift forecasts using an ice ocean model have RMS position errors of 6 km after 24 h
- Position forecasts remain skillful at 9 days after forecast relative to climatology
- Using a sea ice model for image scheduling will substantially increase chances of hitting target

Correspondence to:
A. J. Schweiger,
axel@apl.uw.edu

Citation:
Schweiger, A. J., and J. Zhang (2015), Accuracy of short-term sea ice drift forecasts using a coupled ice-ocean model, *J. Geophys. Res. Oceans*, *120*, 7827–7841, doi:10.1002/2015JC011273.

Received 26 AUG 2015
Accepted 3 NOV 2015
Accepted article online 5 NOV 2015
Published online 12 DEC 2015

Abstract Arctic sea ice drift forecasts of 6 h–9 days for the summer of 2014 are generated using the Marginal Ice Zone Modeling and Assimilation System (MIZMAS); the model is driven by 6 h atmospheric forecasts from the Climate Forecast System (CFSv2). Forecast ice drift speed is compared to drifting buoys and other observational platforms. Forecast positions are compared with actual positions 24 h–8 days since forecast. Forecast results are further compared to those from the forecasts generated using an ice velocity climatology driven by multiyear integrations of the same model. The results are presented in the context of scheduling the acquisition of high-resolution images that need to follow buoys or scientific research platforms. RMS errors for ice speed are on the order of 5 km/d for 24–48 h since forecast using the sea ice model compared with 9 km/d using climatology. Predicted buoy position RMS errors are 6.3 km for 24 h and 14 km for 72 h since forecast. Model biases in ice speed and direction can be reduced by adjusting the air drag coefficient and water turning angle, but the adjustments do not affect verification statistics. This suggests that improved atmospheric forecast forcing may further reduce the forecast errors. The model remains skillful for 8 days. Using the forecast model increases the probability of tracking a target drifting in sea ice with a 10 km × 10 km image from 60 to 95% for a 24 h forecast and from 27 to 73% for a 48 h forecast.

1. Introduction

Economic pressures and decreases in Arctic sea ice over the last 35 years have increased human activity in the Arctic. Tourism, shipping, and exploration for natural resources are on the rise. In addition, many scientific research experiments to advance our understanding of the causes and consequences of sea ice changes are launched every year. These activities often involve operations within or near the sea ice pack making the ability to forecast its evolution over time extremely important. Recent sea ice prediction research has focused largely on seasonal to decadal scales [e.g., *Zhang et al*., 2008a; *Blanchard-Wrigglesworth et al*., 2011; *Stroeve et al*., 2014a] with relatively few studies addressing forecasts on daily and weekly time scales. Surprisingly, short-term sea ice forecasts have received little attention and the literature refers to systems designed several decades ago [*Grumbine*, 1998; *Preller and Posey*, 1989] or those based on forecasts that do not involve a dynamic sea ice ocean model [*Grumbine*, 2013]. Short-term sea ice forecasts have a wide range of applications—from navigation in Arctic waters over marine mammal research to risk assessment for oil extraction platforms.

The motivation for this study is to improve sea ice forecasts to plan and support research experiments. The Marginal Ice Zone (MIZ) Program, funded by the Office of Naval Research, conducted a field experiment in 2014 designed to increase our understanding of processes in the marginal ice zone. As part of this experiment, a campaign was designed to collect a variety of remote sensing data, including high-resolution synthetic aperture radar (SAR) and optical images by classified intelligence satellites (National Technical Means) that provide unclassified Literal Image Derived Products (LDIP) at 1 m resolution [*Kwok and Untersteiner*, 2011]. Researchers use these images to monitor the evolution of the ice pack over the course of the season—documenting, for example, the change in the size distribution of sea ice floes and the coverage of melt ponds on sea ice. Images were required to follow an array of measurement assets deployed by researchers including wave buoys, ice tethered profilers, mass balance buoys, and Seagliders. One problem encountered in the MIZ image acquisition strategy was that image scheduling for both commercial and governmental satellites needed to be done days in advance of the acquisition time. With the relatively small area of coverage offered

by high-resolution sensors (LDIP as small as 10 km × 10 km) and mean daily ice motion of similar magnitude, accurate predictions of ice motion became essential for scheduling image acquisitions. In addition, planning and executing field logistics such as locating ice camps or retrieving equipment would benefit from improved short-term forecasts of sea ice drift. To aid these efforts, we designed a forecast experiment using the Marginal Ice Zone Modeling and Assimilation System (MIZMAS), a coupled ice-ocean model that is derived from the Pan Arctic Ice Ocean Modeling system (PIOMAS). PIOMAS [*Zhang and Rothrock*, 2003] has been used widely for sea ice hindcasts and has been validated extensively [e.g., *Schweiger et al*., 2011]. MIZMAS is a derivative of PIOMAS but features higher spatial resolution for the Chukchi, Beaufort, and Bering seas and is currently undergoing modifications to include prognostic representation of floe size distribution [*Zhang et al*., 2015a]. The results are meant to provide guidance for similar sea ice drift prediction applications and to motivate research into future improvements of short-term sea ice drift forecasts.

2. Methods

2.1. MIZMAS

Our forecast experiment utilizes the current evolving version of MIZMAS (version 1.0), which is being developed to better represent processes in the marginal sea ice zone. MIZMAS is a variant of PIOMAS [*Zhang and Rothrock*, 2003; *Schweiger et al*., 2011] that has a sea ice model coupled to an ocean circulation model. The ocean circulation model is based on the Parallel Ocean Program (POP) developed at Los Alamos National Laboratory [*Smith et al*., 1992]. The POP ocean model was modified by *Zhang and Steele* [2007] so that open boundary conditions can be specified. The POP ocean model was further modified by *Zhang et al*. [2010] to incorporate tidal forcing arising from the eight primary constituents (M_2, S_2, N_2, K_2, K_1, O_1, P_1, and Q_1) [*Gill*, 1982]. The tidal forcing consists of a tide generating potential with corrections due to both the earth tide and self-attraction and loading following *Marchuk and Kagan* [1989].

The sea ice model is a thickness and enthalpy distribution (TED) sea ice model [*Zhang and Rothrock*, 2001; *Hibler*, 1980]. The TED sea ice model has eight categories each for ice thickness, ice enthalpy, and snow depth. The centers of the eight ice thickness categories are 0, 0.38, 1.30, 3.07, 5.97, 10.24, 16.02, and 23.41 m [see *Zhang et al*., 2010, 2015b]. Thus the first category is actually the open water category, while the other seven categories represent ice of various thicknesses. The ice concentration for the grid cell is simply the sum of the area fraction of all categories excluding the open water category. Similar to PIOMAS, it is able to assimilate satellite observations of sea ice concentration following *Lindsay and Zhang* [2006] and sea surface temperature (SST) following *Manda et al*. [2005] and *Schweiger et al*. [2011].

The MIZMAS model domain covers the Northern Hemisphere north of 39°N (Figure 1a). The MIZMAS finite difference grid is based on a generalized orthogonal curvilinear coordinate system with a horizontal dimension of 600 × 300 grid points. The "north pole" of the model grid is placed in Alaska to avoid the singularity at the pole. Thus, MIZMAS has its highest horizontal resolution along the Alaska coast and in the Chukchi, Beaufort, and Bering seas. The model resolution ranges from an average of 4 km along the Alaska coast to an average of ∼10 km for the entire Chukchi and Beaufort seas (Figure 1b). There are 26 ocean grid cells across Bering Strait for a good connection between the Pacific and Arctic oceans. To better resolve the mixed layer and the pycnocline, the ocean's vertical dimension has 40 levels of different thicknesses, with 19 levels in the upper 100 m, the top 16 of which are 5 m thick. The model bathymetry (Figure 1b) is obtained by merging the IBCAO (International Bathymetric Chart of the Arctic Ocean) data set and the ETOPO5 (Earth Topography Five Minute Gridded Elevation Data Set) data set [see *Holland*, 2000].

The modification of the POP ocean model to allow open boundary conditions enables MIZMAS, a regional model, to be one-way nested to a global coupled sea ice-ocean model [*Zhang*, 2005]. The global model's outputs of ocean velocity, temperature, salinity, and sea surface height are used as open boundary conditions for the southern boundaries of the MIZMAS domain along 39°N. Initial conditions for the MIZMAS integration consist of 1 January 1972 fields of sea ice and ocean state variables obtained from a PIOMAS integration that starts from 1948 [*Zhang et al*., 2008b].

2.2. Forcing Data

MIZMAS is routinely driven by daily NCEP/NCAR reanalysis surface atmospheric forcing [*Kalnay et al*., 1996] extracted from NOAA Physical Sciences Division archives. Winds (10 m), downwelling longwave radiation,

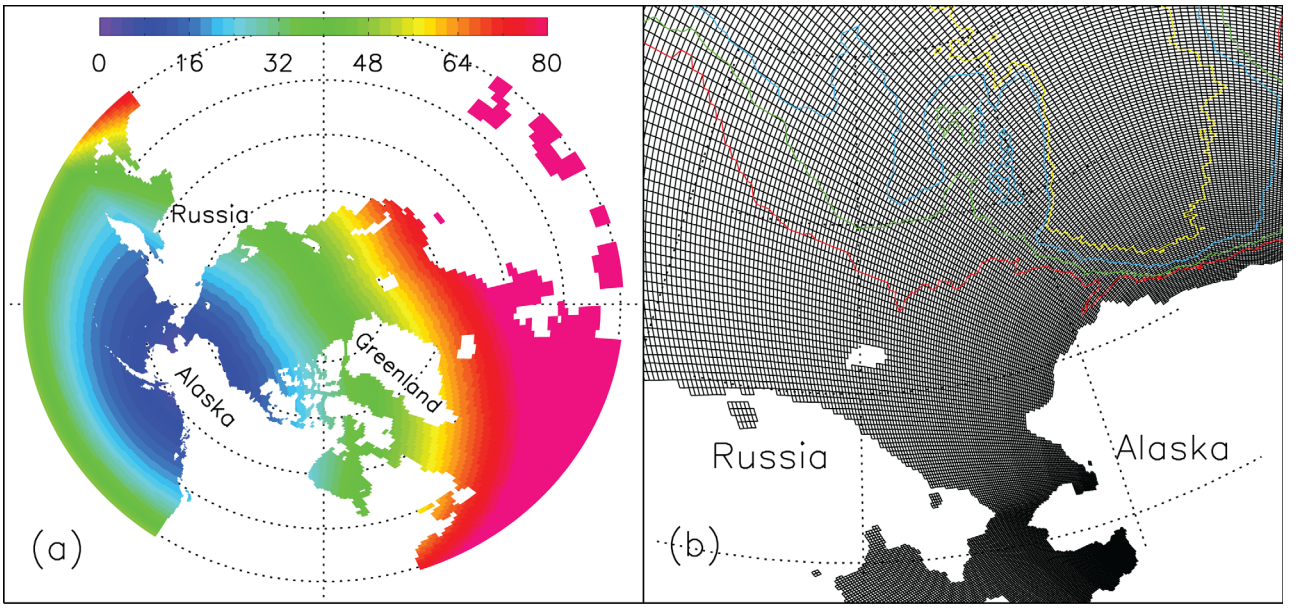

Figure 1. MIZMAS model grid configuration showing (a) the entire model domain consisting of the Arctic, North Pacific, and North Atlantic oceans and (b) the subdomain of the Chukchi, Beaufort, and East Siberian seas. The model domain covers all ocean areas north of 39°N. The colors in Figure 1a indicate the model's varying horizontal resolution in km (see color key at top of figure). In Figure 1b, the red, green, blue, and yellow lines represent isobaths of 100, 500, 2200, and 3600 m, respectively.

surface radiation, and precipitation are extracted from NOAA and drawn on the MIZMAS curvilinear grid. Downwelling shortwave radiation is calculated from NCEP/NCAR cloud fraction and specific humidity using a parameterization from *Parkinson and Washington* [1979]. The model is integrated from 1 January 1971 up to the day of the forecast. Forcing data for the forecast period are obtained from the NCEP Climate Forecast System (CFSv2) [*Saha et al.*, 2014], which provides an ensemble forecast at 6 h increments for up to 9 months. For the limited scope of this experiment, a single ensemble member (member 2) was arbitrarily chosen to drive the ice forecast. Because our experiment includes a series of initialization times and evaluations for many locations, essentially providing an ensemble of initializations, there is no need to run simulations with multiple atmospheric realizations. Forcing variables, 10 m winds, downwelling shortwave and longwave radiation, specific humidity, and surface temperature at 2 m were extracted at 6 h intervals. P-E was calculated from precipitation rates and evaporation calculated from CFSv2 latent heat fluxes. All variables were regridded to the MIZMAS curvilinear grid.

The transition from NCEP/NCAR to CFSv2 forcing data was necessitated by the short development time; retroactive integrations using the CFSv2 data would have caused substantial delays. In addition, MIZMAS hindcasts using NCEP/NCAR forcing have been validated extensively against in situ and remote sensing data including 2014 observations from IceBridge [*Zhang et al.*, 2015b]; the initial model state is robust. A comparison of NCEP/NCAR Reanalysis and CFS forecasts shows correlations of 0.93 at the initial time and virtually no bias in wind speed and direction, further justifying the transition from NCEP/NCAR to CFS in this experiment. Due to the short forecast ranges under investigation, systematic differences in the surface energy balance variables for NCEP/NCAR and CFSv2 atmospheric forcing are not expected.

2.3. Forecast Scheme

Forecasts are generally initialized daily from 17 July 2014 to 17 September 2014 with forecast increments of 6 h. The initial sea ice model forecast uses CFSv2 forecast fields valid for 6:00 UTC; the last forecast is run for 6:00 UTC, 9 days later. Over this period a total of 38, 9 day forecasts were initialized, with several daily forecasts missing when research staff were busy with other tasks. Though the initial purpose of the experiment was to support image acquisition for a specific field experiment in the Beaufort Sea, to increase the number of data points and statistical representativeness of the results we expanded the validation and include pan-arctic sea ice drift measurements.

2.4. Buoy Data for Drift Assessment

Buoy data were extracted from the archive of the International Arctic Buoy Program (IABP) between 17 July and 25 September 2014. Data were only available without prior quality assurance so some preprocessing was necessary. Raw satellite transmissions from buoys frequently have erroneous sections. For example, a buoy may be turned on for transmission while still on a ship or aircraft or may be repositioned in the middle of its trajectory. In addition, raw buoy trajectories may have displacement errors due to data transmission errors. To deal with these issues, we applied a maximum speed filter of 100 km/d, applied a temporal median filter on position, and inspected trajectories visually to identify buoys that may have become locked in fast ice or beached. Buoy positions were then interpolated linearly in time to the 6 h intervals of the model forecast. For the initial model time step, ice velocity components u,v from the model are interpolated bi-linearly to the initial buoy position and the next model trajectory position is calculated. Subsequent model-trajectory positions are then computed using the previous model-trajectory point as the initial position. Because our investigation tracks targets that are located in ice-covered areas rather than buoys drifting in open water, we eliminate part of any trajectory that was in open water based on the ice thickness data generated by the model. After the filtering, 128 separate buoy tracks that could be used for validation of our forecasts remained in our database (Figure 2).

2.5. Validation Methods

Our approach is to compare forecast buoy trajectories with observed trajectories and compute validation statistics that provide information on how well the forecasts capture the observed speed and position. It is useful to consider forecast accuracy compared to a reference or an alternate way of making the forecasts. In weather forecasting, persistence and climatology are often used as the reference to which forecasts are compared. This provides information about the relative gain a particular forecast achieves over something that might be simpler, cheaper, or more readily accessible and thus gives an indication of the relative benefit to cost.

Here we select as reference the mean ice motion fields generated by integrations of MIZMAS from 2003 to 2013 using forcing from the NCEP/NCAR reanalysis, which was also used to initialize the model. Daily ice velocity fields are averaged from July through September yielding a mean daily ice velocity corresponding to each day of our forecast experiment. We call this the "climatological ice motion" field although the period is too short to be considered a "climatology." Trajectories are computed for each of the buoys from the climatological velocity field. A new trajectory is initialized for each of the forecast experiment days so that the resulting "climatology" trajectories can be paired with "forecast" trajectories. Because forecast fields have a 6 h time resolution, while mean fields have a 24 h resolution, trajectories computed from these fields also have 6 and 24 h time resolution for forecast and "climatology" trajectories, respectively.

Mean velocity fields, such as those generated by the IABP program [*Rigor et al.*, 2000], could have been used as reference instead of model generated climatological fields. Those buoy mean velocity fields, however, because they are based on optimally interpolated buoy motions, would have been smoothed spatially and temporally; they would present little challenge for our forecast system. A more challenging reference would have been to use sea ice drift forecasts produced operationally by NCEP [*Grumbine*, 1998], which are based on an empirical relationship between sea ice drift and geostrophic winds. We will discuss our forecast results relative to those published for the NCEP operational system [*Grumbine*, 1998, 2013]. Persistence was not considered as a reference because, given the rotating climatological ice motion pattern in the Amerasian basin, a linear extrapolation of the initial motion would take the computed trajectory quickly away from the climatological trajectory.

3. Results

3.1. Comparison of Speed Errors

We begin validation by comparing forecast model speeds to corresponding buoy speeds. Speeds are calculated from the daily 24 h displacements in forecast and observed buoy trajectories. To better highlight the decay in forecast quality with forecast time, we examine daily ice speeds for forecast increments rather than average speeds over the entire forecast interval. Validation statistics for different forecast validation times ranging from 24 h since forecast, to 216 h (9 days) are given. Figure 3 shows root mean square (RMS) speed errors for trajectories from forecast experiments and from trajectories calculated using the mean ice motion field (climatology) over the period. Speed RMS errors for forecasts are on the order of 4.5–5 km/d

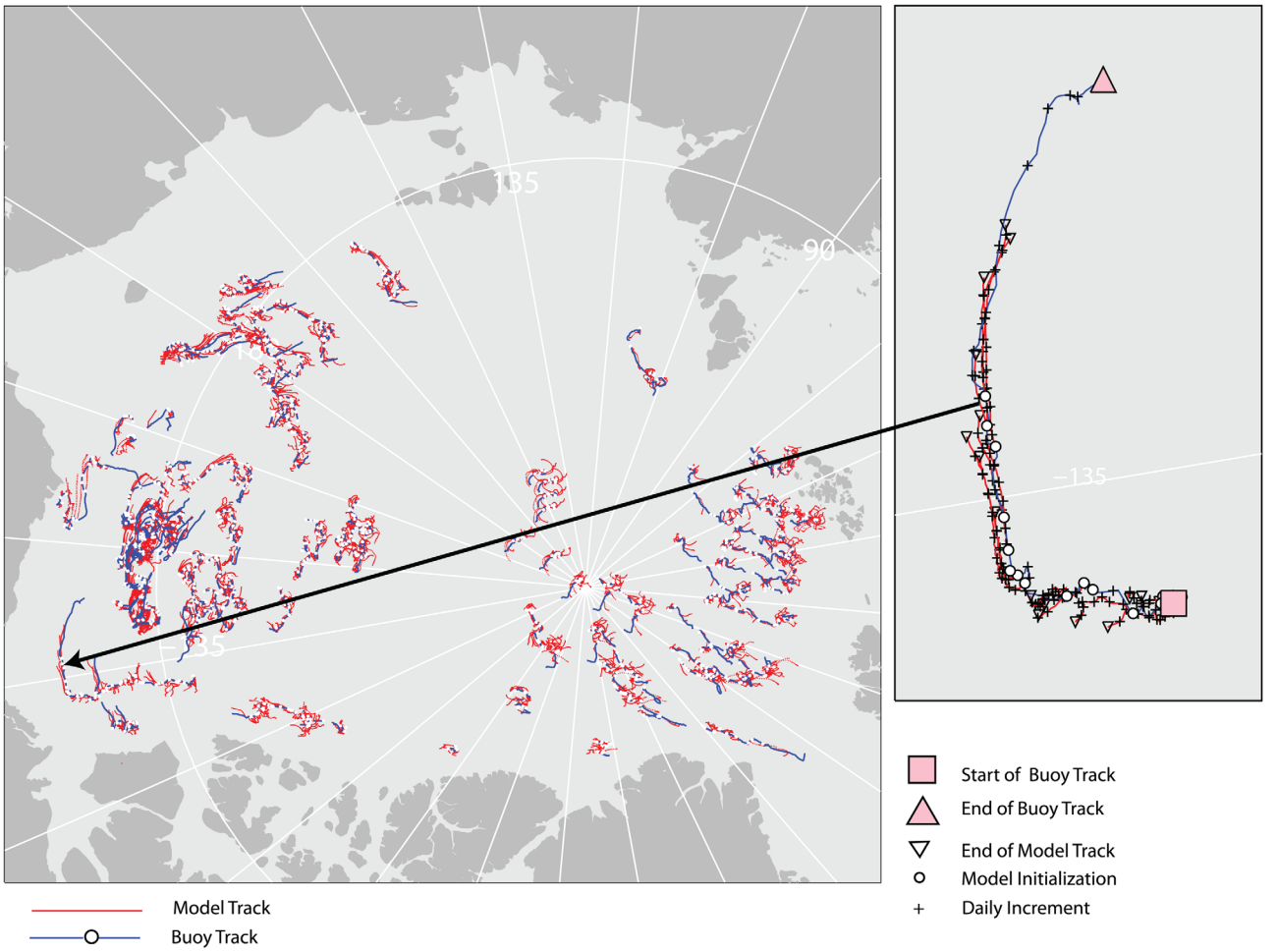

Figure 2. Map of buoy (blue) and model tracks used in the assessment of position and speed forecasts. Right side shows observed and modeled track for a single buoy pointed to by the black arrow. The pink square marks the beginning of the buoy track, and pink triangle marks the end of the buoy track. White circles mark the initialization location and small downward triangles mark the end of forecast (usually 9 days). Black plus symbols mark daily increments.

for up to 72 h since forecast, then rise to 8 km/d at 9 days since forecast. This compares with RMS speed errors for trajectories computed from climatological velocity fields that are on the order of 9 km/d and expectedly independent of forecast time. The fact that RMS speed errors for the forecast trajectories remain less than the errors for the climatology trajectories indicates that the forecasts are somewhat skillful with respect to speed at times when we would expect the skill of the CFS forecast model to have decayed completely (9 days). A simple explanation for this may be that because of the initial skill of the forecast, the forecast trajectory remains closer to the observed trajectory than the climatology trajectory, and is therefore more likely subject to the same wind and ice conditions as the buoy. Therefore, forecast speeds at 9 days remain better than climatology.

To assess the quality of the forecast relative to the reference system (climatological ice motion), we compute a skill score (SS) that provides a measure of the reduced variance of the forecast relative to the reference system. The SS is defined as

$$SS = 1 - \frac{MSE_{forecast}}{MSE_{Mean}}, \tag{1}$$

$$MSE = \frac{\sum^{N} \left(U_{Predicted} - U_{Buoy}\right)^2}{N}, \tag{2}$$

with the mean squared errors ($MSE_{forecast}$ *and* MSE_{mean}) computed from $U_{predicted}$, the predicted speeds using trajectories from the forecast or climatology velocity fields, respectively. U_{buoy} gives the observed speeds,

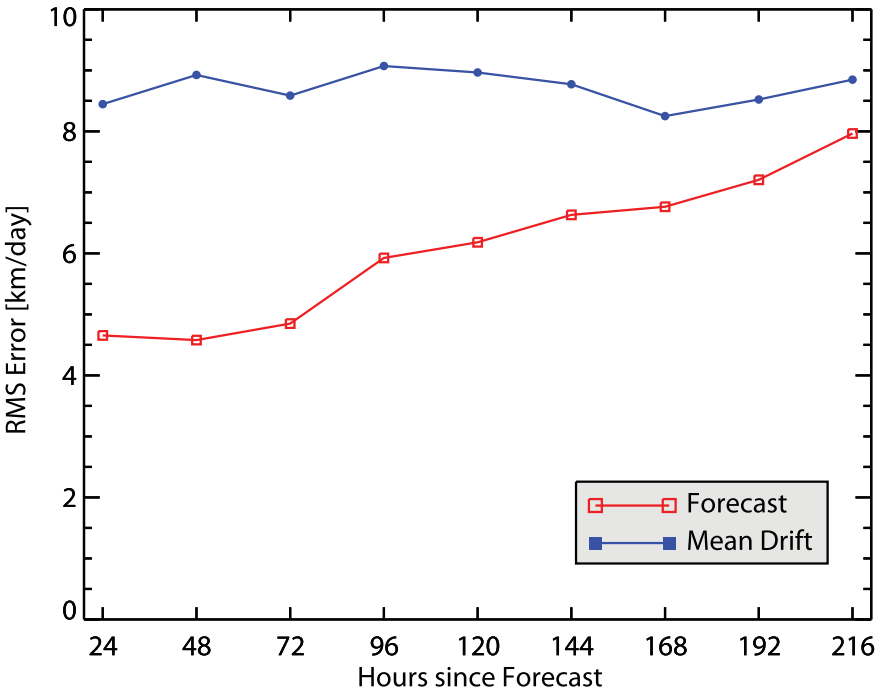

Figure 3. RMS error of drift speed for forecast (red) and mean drift (blue). RMS error is given for different forecast validation times from 24 h since forecast up to 216 h from forecast.

and *N* the number of forecast and observation periods. The SS provides a measure of how much variance of the error is reduced by the forecast relative to the climatology reference. A perfect forecast would have a value of 1; a forecast that provides no benefit over the reference would have a skill score of 0. Skill scores are only computed for 24 h forecast intervals because climatological trajectories are only available for 24 h intervals. Figure 4 shows the forecast skill for drift speed relative to the drift speed predicted using mean velocity fields. Forecast skill is high, above 70% of reduced variance, for 24–72 h since forecast with a small increase from 24 to 48 h. Skill scores after 72 h decline gradually but remain at 20% after 9 days since forecast.

3.2. Comparison of Position Errors

For our particular application, the scheduling and targeting of image acquisitions, the accuracy of forecast position is the most relevant parameter. For high-resolution images that may only cover a 10 km × 10 km area, error in the forecast position may result in reduced overlap with the target or could result in missing the target altogether. For images that have to be purchased this can be a costly error; it is also a lost opportunity to view important changes in the physics of the target area.

To characterize the position error of the forecast, we follow a similar strategy as for speed errors and compare positions that are forecast using our forecast model, positions that are forecast using climatological ice motion fields, and observed buoy positions. Figure 5 shows the RMS position errors calculated from the geometric distance between forecast position and actual position predicted by the forecast model and by using climatological velocity fields. Forecast model RMS errors increase rapidly to about 6 km after 24 h since forecast. Position errors for predictions based on climatology are 12 km. The relative improvement in RMS position error that is gained by using the forecast model over a forecast based on climatology is on the order of 50% up to 96 h since forecast, decreasing to about 35% at 8 days. Figure 4 also shows the SS for position of the forecast relative to climatology. Scores are above 70% of reduced error variance up to 120 h, remaining just below 60% at 8 days since forecast. This persistence in skill for position is due to the initial skill of the forecast that is propagated, rather than the ability to forecast ice motion at 9 days in advance. A buoy whose position was forecast well for a few days will be closer to its actual position after 9 days, even though the daily (wind) forecast itself has lost nearly all predictive power. This is a result with practical application. Mean position errors at 24 h since forecast are 5 and 10 km, and 32 and 53 km after

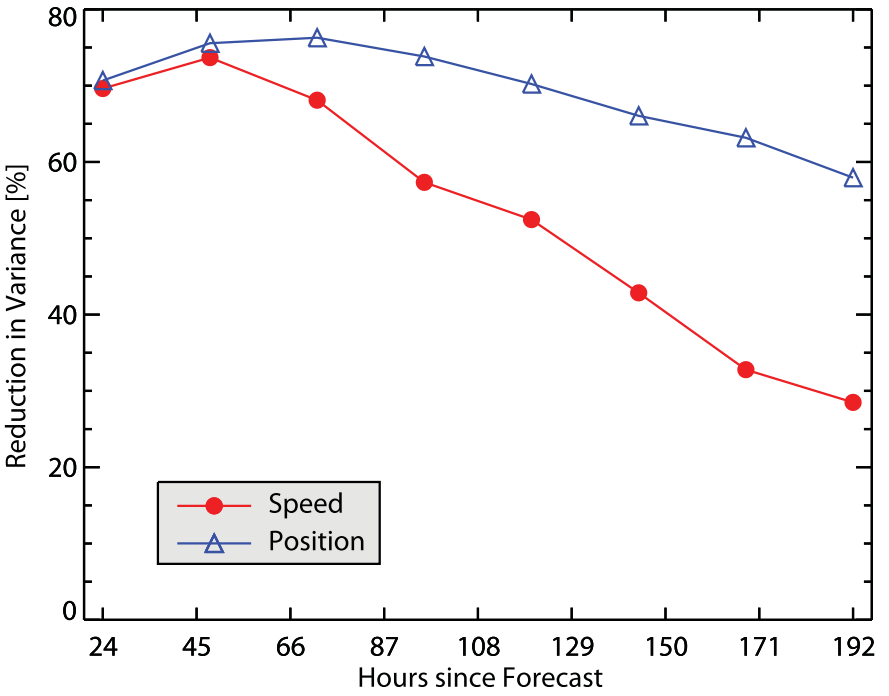

Figure 4. Forecast skill scores for buoy drift speed (red) and position (blue) relative to drifts predicted using mean ice velocity fields.

8 days for the model forecast and climatology, respectively. An inspection of the distribution of position errors (Figure 6) provides a practical perspective on the relative improvement achieved by the forecast model over a prediction using climatology. Using the 10 km target size (e.g., the scene size of an LDIP image) as a criterion, there is a 60% probability (intersection of cumulative curve with 10 km position error)

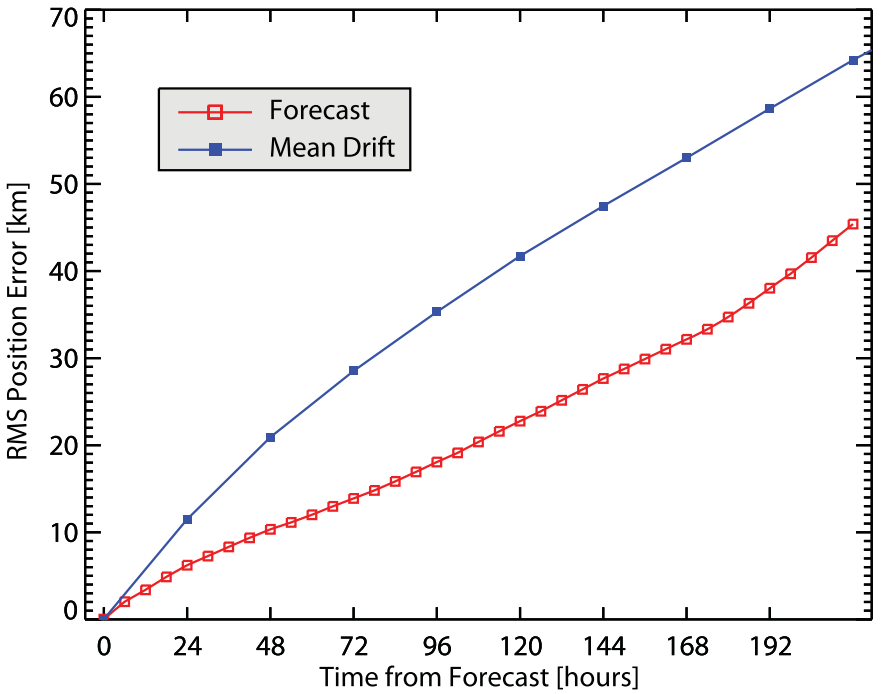

Figure 5. RMS position errors at different forecast times for positions predicted by the model forecast (red) and positions predicted by using mean daily velocity fields (climatology) in blue.

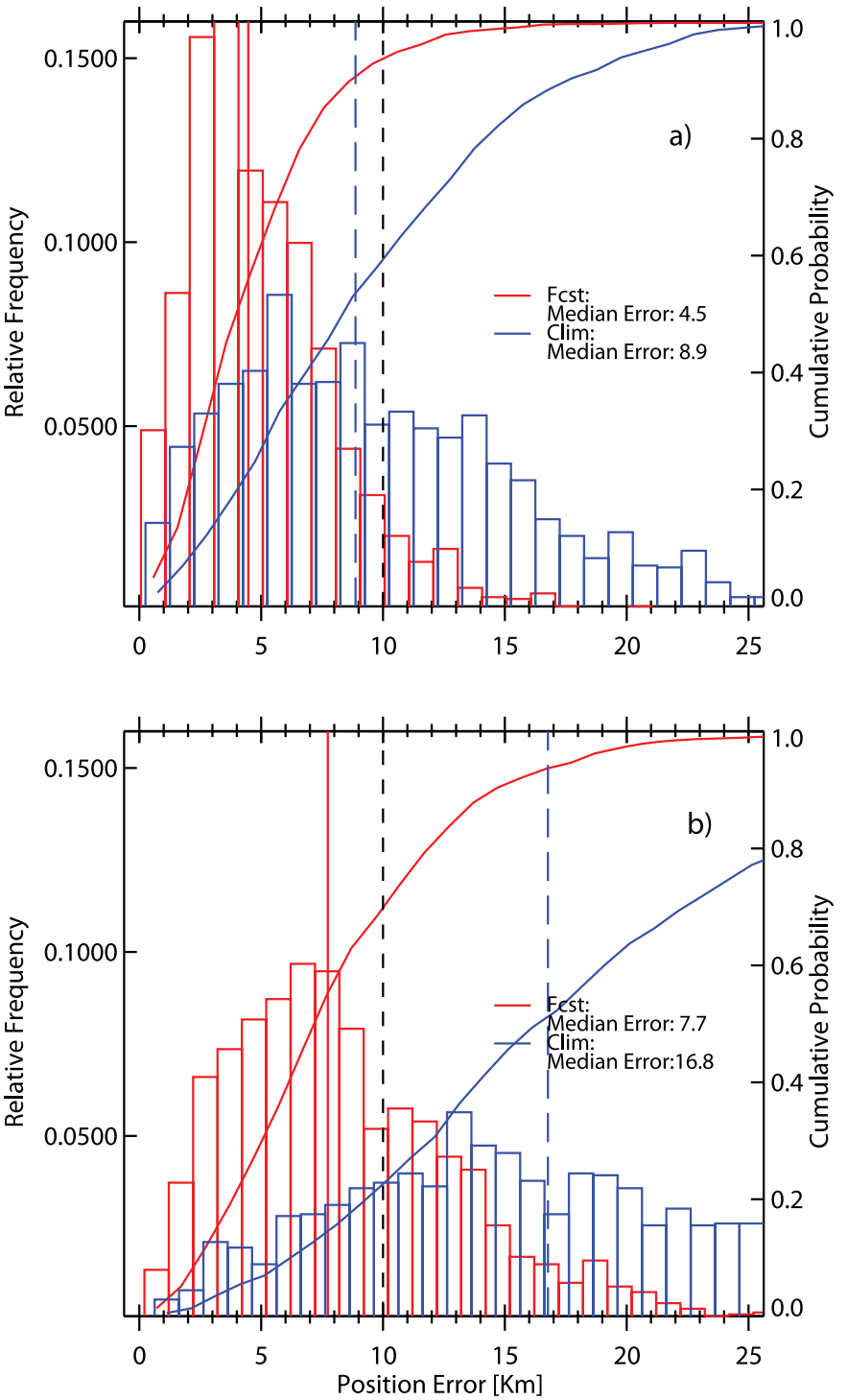

Figure 6. Histogram of position errors for the forecast model (red) and for positions (blue) predicted using climatology for (a) 24 h after forecast and (b) 48 h after forecast. Solid curves indicate cumulative probabilities. Vertical lines show median errors for forecast and climatology, respectively.

of forecasts made using the climatology velocity field that would have been within 10 km of the actual position after 24 h. This value rises to 95% using the model forecast. After 48 h the probability of imaging a target when using the forecast model is still 75% compared with only 27% using climatology. Even after 5 days, a 30% chance of hitting a target remains using the forecast while it is close to zero using climatology.

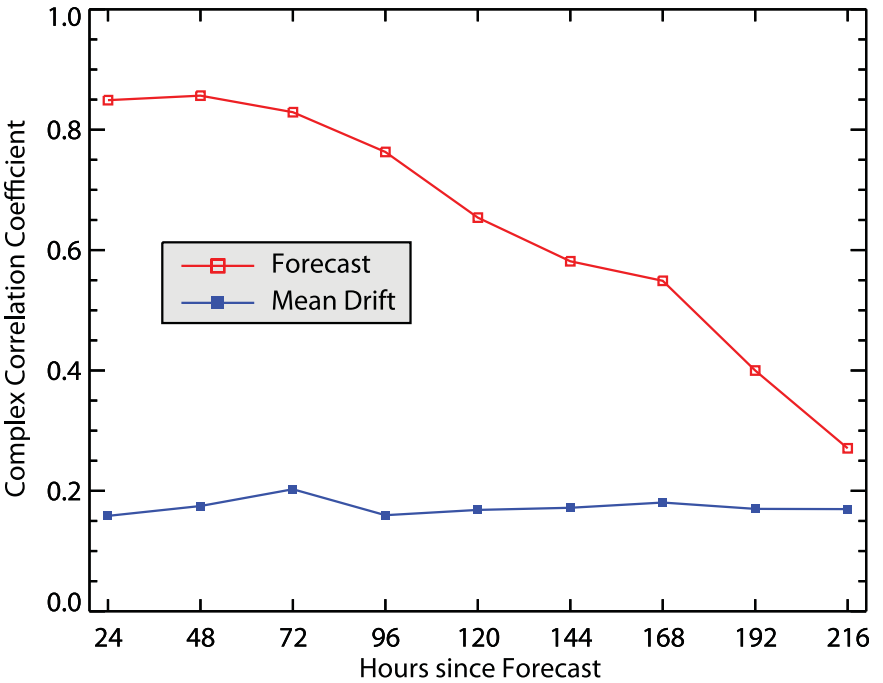

Figure 7. Correlation coefficient *r* resulting from fitting observed and modeled velocities using the linear model.

3.3. Tuning

Although the above results are encouraging and clearly demonstrate the value of the model-based forecast over predicting speed or position from climatology, we ask the question about how to best improve the forecast. To do this we examine the errors in drift for any systematic errors that may provide clues. Following *Thomas* [1999] we fit a simple model to observed and modeled velocities:

$$U_{Observed} = AU_{model} + D + E, \tag{3}$$

where U_{observed} and U_{model} are the observed and modeled vector velocities and A and D are complex coefficients calculated by minimizing the error E. The method, implemented as a complex linear fit, also provides a scalar regression coefficient r. This method is a convenient way to examine vector relationships and the computed coefficients are a measure of whether linear adjustments in magnitude and direction of the vectors are likely to remove biases. Figure 7 shows the correlation coefficient r resulting from the regression of $U_{observed}$ and $U_{modeled}$. As expected from prior comparisons of buoy and model speeds, the correlation is very high with values of 0.85 at 72 h since forecast, indicating 70% of the variance in observed buoy velocities is captured by this linear model.

The estimated coefficients A and D are used to evaluate this model at mean velocities and to estimate speed and turning angle biases between observed and modeled trajectories. Buoy mean speed at 10 km/d is about 10% faster than the corresponding model drift and the model drifts tend to be about 5° to the left of the observed drift (Figure 8). The distribution of drift angles computed as the vector difference between model and observed ice at 24 h since forecast has a mean of −3.5° and a median of −3.3° with increasing scatter and longer lags (Figure 9). The increasing interquartile range after 96 h since forecast is another indication of the decay of the forecast skill.

Ice motion is determined by the following momentum balance [*Hibler*, 1979]:

$$m\,\partial\mathbf{u}/\partial t = -m\bar{f}\mathbf{k}\times\mathbf{u} + \boldsymbol{\tau}_\mathbf{a} + \boldsymbol{\tau}_\mathbf{w} - mg\nabla_H p(0) + \nabla\cdot\sigma, \tag{4}$$

where m is ice mass per unit area, $\mathbf{u}$ is ice velocity, $\bar{f}$ is the Coriolis parameter, $\mathbf{k}$ is the unit vector in the z direction, $\boldsymbol{\tau}_\mathbf{a}$ is air drag, $\boldsymbol{\tau}_\mathbf{w}$ is water drag, g is the acceleration due to gravity, $p(0)$ is sea surface dynamic height, and σ is ice internal stress tensor (σ_{ij}). The air and water drag are

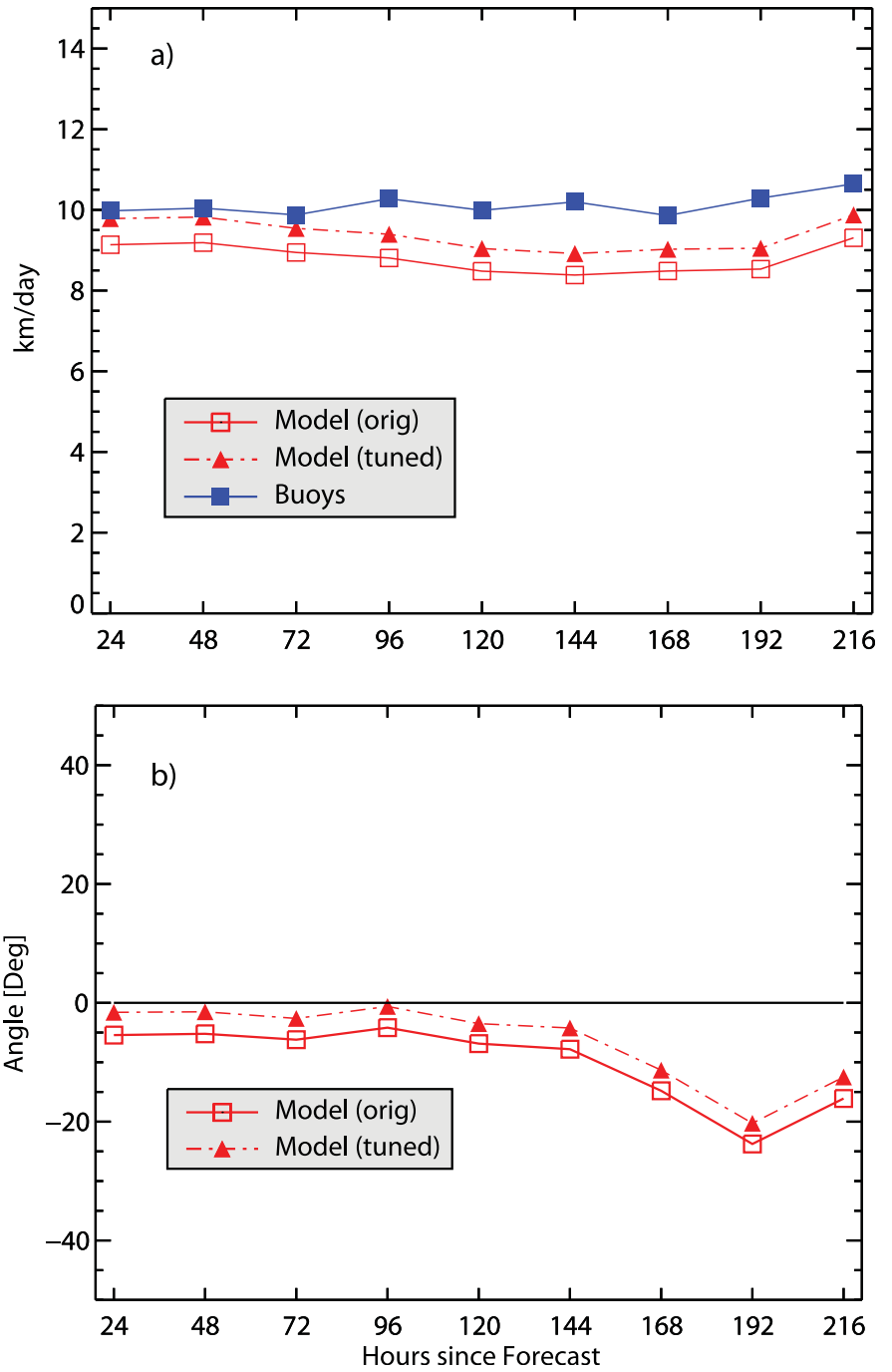

Figure 8. (a) Mean ice speed for model, original and tuned forecast (red) and buoy observations (blue). (b) Turning angle at mean speed for original and tuned forecast after adjusting water stress turning angle and air drag coefficient. Negative turning angles indicate that the model drift is to the left of the observed drift.

$$\tau_{\boldsymbol{a}} = \rho_a C_a |\boldsymbol{U_a}| (\boldsymbol{U_a} \cos\phi + \boldsymbol{k} \times \boldsymbol{U_a} \sin\phi), \tag{5}$$

$$\tau_{\boldsymbol{w}} = \rho_w C_w |(\boldsymbol{U_w} - \mathbf{u})| [(\boldsymbol{U_w} - \mathbf{u}) \cos\theta + \boldsymbol{k} \times (\boldsymbol{U_w} - \mathbf{u}) \sin\theta], \tag{6}$$

where $\boldsymbol{U_a}$ is surface (10 m) wind, $\boldsymbol{U_w}$ the geostrophic ocean current, ρ_a and ρ_w air and water densities, C_a and C_w air and water drag coefficients, and ϕ and θ air and water turning angles. Here the geostrophic ocean current (under the ocean mixed layer) is taken to be at the seventh level of the ocean model at a depth of 30–35 m. The geostrophic current taken at this depth is appropriate given that the Arctic Ocean mixed layer is often within the depths 5–30 m in summer and has been shoaling in recent years [*Peralta-Ferriz and*

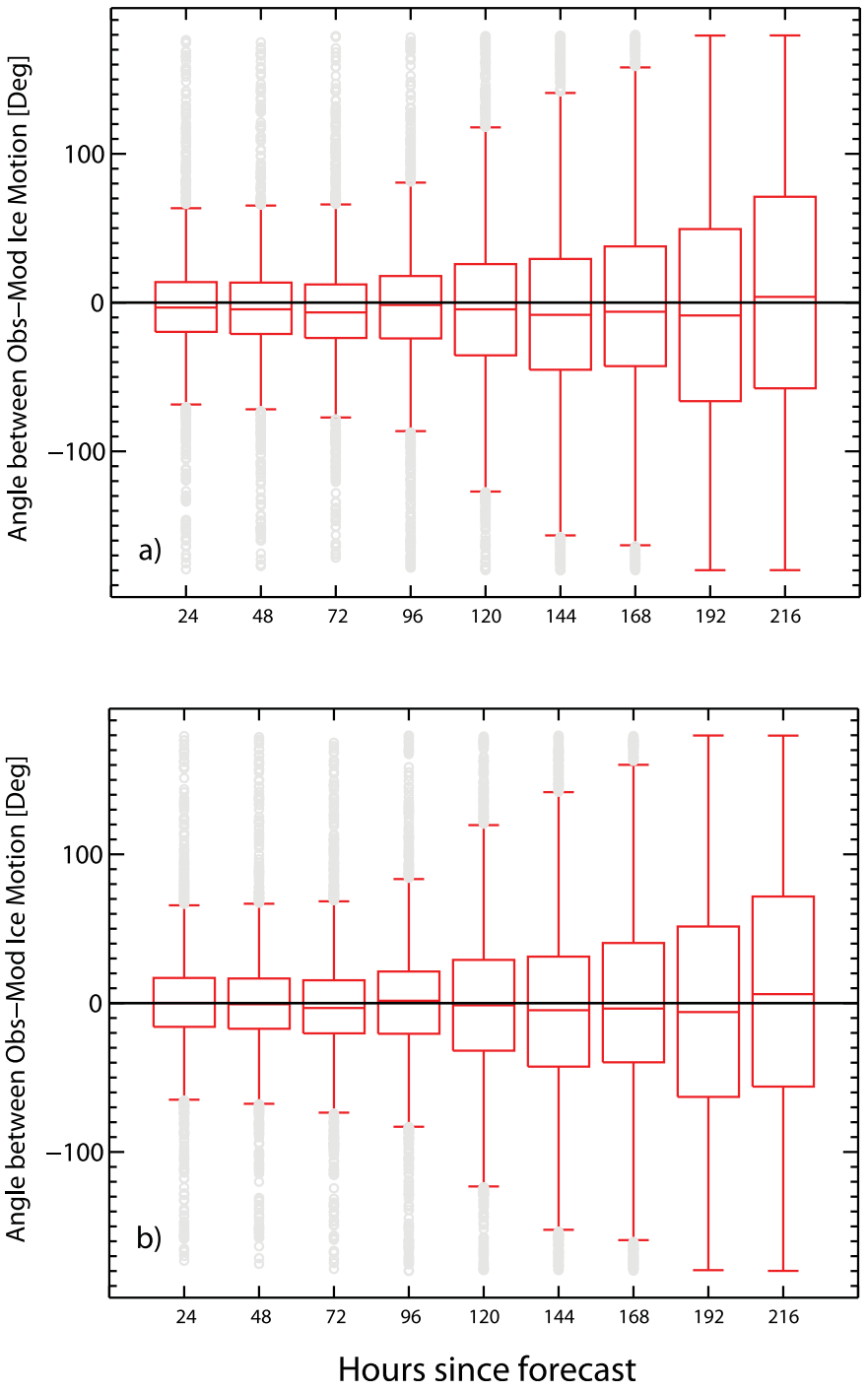

Figure 9. Boxplot showing distribution of angle differences between (a) original and (b) tuned model experiments. Box shows 25 and 75% quartile range. Whiskers provide 1.5 times the 25 and 75% range and values beyond are shown in gray.

Woodgate, 2015]. Following *Hibler* [1979] ice velocity **u** is neglected in (5) because it is an order of magnitude smaller than $\boldsymbol{U_a}$. The air turning angle θ is set to zero because of 10 m winds, which are assumed to have the same direction as the surface wind. The water drag coefficient is set to 0.0055 [*Hibler*, 1979]. Initial values are used for C_a (0.0033) and θ (25°), which are modified in the tuning process to reduce model misfit (see below).

Uncertainties in any of the terms in the momentum balance can lead to biases in the resulting ice velocities. A detailed analysis of the causes is beyond the scope of this paper. An improvement can be achieved relatively simply by applying a scaling and rotation to either the surface wind stress or the ocean stress. This

type of adjustment is made routinely in sea ice model applications and is part of a normal tuning process [*Kreyscher et al*., 2000; *Zhang et al*., 2012], reflecting uncertainties in these parameters. For example, IABP buoy drifts have been used to adjust ice speed (though not angles) to tune PIOMAS to run with atmospheric forcing fields from different reanalyses [*Lindsay et al*., 2014].

To remove these biases, we interactively apply different rotations θ to the ocean stress and increase the air drag coefficient (C_a) to increase model velocities and compare the resulting model biases in speed and angle relative to the observations. Using this optimization we arrive at an air drag coefficient of 0.0036 (increased from a default 0.0033) and a turning angle applied to the water stress of 30°. This turning angle value represents a 5° increase relative to the 25° rotation suggested by *Hibler* [1979]. Using these values reduces the angular and speed biases to near 0, eliminating nearly all systematic biases for this data set (Figures 8 and 9). Despite the removal of these biases, verification statistics for position prediction are changed insignificantly with no discernable improvement in any of the forecast verification statistics. This suggests that overall forecast errors are dominated by other factors and that the small biases in speed and direction do not affect forecast quality. However, larger errors in the rotation of water and wind stress can be important. In an earlier experiment in which the water turning angle (θ) was set to 0 we noticed a substantial (20%) increase in the 24 h forecast position errors. This highlights the sensitivity of ice motion to the water turning angle.

Although the tuning of water stress and wind stress changes forecast verification statistics little, the question remains why a systematic rotation is necessary and whether a change in wind and water stress is better supported by evidence. To find a source of the angular bias between modeled and observed trajectories, we compare observed 10 m winds from the Surface Heat and Energy Budget Experiment (SHEBA) [*Persson et al*., 2002] and those from the NOAA Climate Forecast and ReForecast system (CFSR) [*Saha et al*., 2010], which is an atmospheric reanalysis using the same model as the CFSv2. Data are compared for the SHEBA drift from November 1997 through October of 1998 [*Persson et al*., 2002]. Wind direction data are fairly noisy and are subject to measurement errors and atmospheric modeling errors. To focus on the angular bias, we remove cases with large wind speed differences ($>$2 standard deviations) and angle differences of greater than 50° and consider those clear forecast and reanalysis failures or measurement errors. Wind speed errors, after filtering, are small, with median observed speeds 0.25 m/s greater than CFSR wind speeds, providing justification for an increase in the surface air drag. Mean differences in wind direction between observed and CFSR 10 m winds, however, show CSFR rotated clockwise by 3° $\pm$ 1° from the observed wind. This is the opposite direction from that needed to explain the model bias in ice motion relative to observations. This suggests that the source of the ice motion direction bias does not originate in the surface winds but is likely related to other components of the force balance such as the water stress or the ice interaction force. Because wind direction errors are affected both by errors in the reanalysis (a slight shift in the pressure centers can lead to substantial differences in wind direction) and measurement errors, they tend to be noisy. Although a standard error of $\pm$1 suggests that the estimate is robust, this error estimate is sensitive to the elimination of the extreme outliers described above. *Persson* [2011], using the same wind speed data but comparing them to ERA-40 reanalysis data, also reports a bias in reanalysis wind direction clockwise to the right of observed winds. Eliminating the wind stress as the likely source of the drift bias, we therefore use the water stress tuning approach for future forecasts. Water turning angles measured at ice tethered buoys [*Cole et al*., 2014] suggest a 30° turning angle between the surface and 35 m within the range of possibilities. A more detailed investigation constraining both water and wind stress angles through measurements in multiple locations reflecting different sea ice conditions should be done in the future. Improved representations of ocean and atmospheric boundary layers below and above the ice may further reduce the need for tuning.

4. Discussion and Conclusions

The primary goal of this experiment is to assess the role short-term sea ice forecasts have in planning and executing research projects and to motivate the question of how short-term forecasts might be improved through advances in the sea ice model, the atmospheric model, or the coupling. Our results show that RMS errors for forecast drift speeds rise from less than 4.5 km/d at 24 h since forecast to 8 km/d at 9 days. Velocity vector correlation coefficients are high with values above 0.82 for the first 72 h since forecast. Forecast skill scores for speed are in the range of 70% relative to predictions based on climatology out to 72 h since forecast with model forecasts remaining skillful at the 20% level as late as 9 days since forecast. The ability of the forecast to predict the

future position of a point target is measured by comparing distances between predicted position and observed position for buoys drifting in Arctic sea ice. RMS errors for positions are on the order of 6.0 km at 24 h since forecast rising to 38 km after 8 days. An analysis of systematic errors between observed and forecast trajectories indicates that the model is biased slow by about 10% and displays a 5° drift bias to the left of observed buoy trajectories. After adjusting the air drag coefficient and applying rotations to the water stress on ice, these biases can be reduced to near 0. These adjustments have no effect on forecast verification statistics suggesting that forecast errors are dominated by other sources such as the atmospheric forecasts. Although these errors are not small relative to average daily displacements, which have a mean value of 10 km, using the model-based forecast instead of one using mean sea ice velocities increases the probability of finding a target, such as a field camp, in a high-resolution satellite image sized 10 km × 10 km, from 60 to 95% at 24 h since forecast and from 27 to 75% after 48 h. Even after 5 days when atmospheric forecast skill has decayed, the chance of finding the target is still 30% using the forecast model compared with nearly zero for using climatology. Using a forecast system such as the one examined here is well indicated in target acquisition applications.

Forecasts errors established in these limited experiments can be compared to other sea ice forecast experiments. *Grumbine* [1998, 2013] compares ice drift forecasts generated from wind forecasts and an empirical free drift sea ice model [*Thorndike and Colony*, 1982]. *Grumbine* [1998, 2013] reports correlations and RMS errors for distance (equivalent to speed in km/d) for different forecast times. Results show a scalar correlation coefficient for distance of less than 0.47 for 24 h forecasts over the period 1993–1995 [*Grumbine*, 1998]. Recently, *Grumbine* [2013] used an updated forecast model and a larger validation data set spanning 1998–2007 and reports scalar speed correlations less than 0.4. Scalar speed correlations reported here are much higher, with 24–48 h correlations on the order of 0.7. Position errors (RMS error radius) reported by *Grumbine* [2013] are smaller, 5 km at 24 h since forecast compared with 6 km reported here, and about the same (40 and 38 km, respectively) at 9 days since forecast.

This raises the question whether a coupled ice-ocean model will yield improved forecasts over an empirical free drift model. Using a simple linear free drift model with coefficients fit to the data set of observed motion and the CFS winds used in this forecast experiment yields an RMS speed error of 5 km/d at 24 h since forecast. This compares with the 24 h RMS speed error of 4.5 km/d from MIZMAS, a slight improvement. A prior study compared a free drift model with an earlier version of the ice-ocean model that evolved into MIZMAS [*Thomas*, 1999] and reports RMS velocity errors for daily hindcasts to be less (6.3 km/d) than those using a coupled sea ice model (7.7 km/d), suggesting that an empirical free drift model performs better. The results presented here, though limited in scope, suggest that improvements in the sea ice model now yield similar or better results than the linear drift model. This result must be understood in the context of sea ice that has sped up in recent years [*Rampal et al*., 2009] due to changes in ice thickness and strength [*Zhang et al*., 2012; *Olason and Notz*, 2014]; mean ice speeds are now nearly twice as high as only two decades ago. Thus, the relative errors in ice drift speed have decreased even more. A more comprehensive comparison of the approaches including different ice and atmospheric models would have to answer the question whether a free drift forecast can still outperform a dynamic sea ice model. The benefits of a dynamic model over a simple free drift model may be limited to specific situations. For example, strong ice motion and deformation during the passage of storms or increases in ice velocities due to rapid thinning and associated reductions in ice strength might be better captured by a model that explicitly simulates such effects. In addition, we expect a coupled system that can account for the physical variations in the coupling between atmosphere, ice, and ocean such as the variations in ice thickness, surface roughness, and ice and ocean drag, to ultimately provide superior solutions.

RMS position errors must also be understood in the context of model resolution; here, 24 h errors are about half the average model resolution. Because the MIZMAS curvelinear grid has varying grid cell sizes, it is possible to investigate the role of model resolution on results. An examination of errors just for the Beaufort and Chukchi seas, where the model grid has a typical size of 4 km, shows that errors for speed and positions are nearly identical to those for the entire basin. This suggests that sampling errors due to the finite resolution of the model are not the primary source of forecast errors and that increases in model resolution may not necessarily yield improved results. But the role of model resolution is more complicated and an increase in ice model resolution without an increase in resolution of the atmospheric forcing is not likely to yield improved results. *Grumbine* [2013], in examining the sensitivity of sea ice drift forecasts using surface winds from the Global Forecast System (GFS), reports that reductions in velocity errors due to resolution follow a step function. Therefore, a more detailed analysis across a range of resolutions in both atmospheric forecast models and the sea ice model would have to examine the effects of resolution. A direct analysis that uses

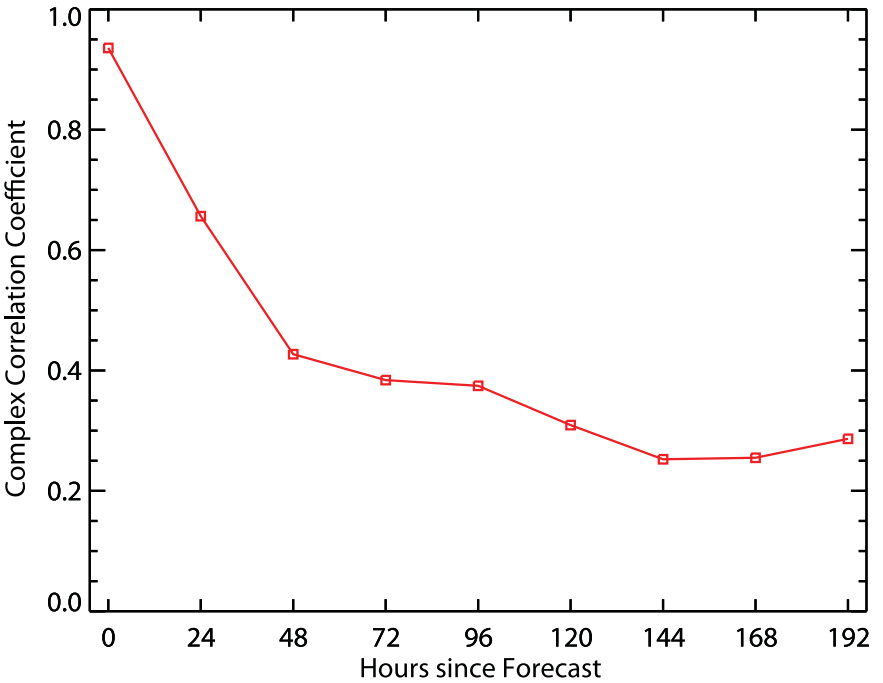

Figure 10. Correlation coefficient between wind velocity between CFS-V2 forecast and NCEP/NCAR reanalysis.

the same validation and forcing data and separates the effects of forcing data and the sea ice model would have to answer the question whether a coupled dynamic ice-ocean model offers any substantial benefits over those generated by a free drift model. An intercomparison with other sea ice forecast systems such as the US-Navy Arctic Now and Forecast System (ACNFS) [*Posey et al.*, 2015] would also be useful.

The relatively large magnitude of velocity errors relative to mean velocity (60%) even at short forecast times (24 h) raises the question of the path forward for improvements in short-term sea ice forecasts. Figure 10 shows the decay in correlation between CFS forecast and NCEP reanalysis over the forecast period (across entire grid). As expected, correlations are nearly perfect at 0 lag but decrease quickly to only 0.65 at 24 h since forecast. In our forecast experiment 10 m winds explain over 90% of the modeled sea ice motion at 24 h, which suggests that improvements in wind forecasts are likely the most important route for drift forecast improvement. A recent study of vertical wind profiles from dropsondes deployed over sea ice in the Beaufort Sea during summer 2014 [*Liu et al.*, 2014] suggests that improvement in vertical mixing schemes are also indicated. A denser network of upper air stations near the Arctic Ocean may also have a role in improving wind forecasts.

References

Blanchard-Wrigglesworth, E., C. M. Bitz, and M. M. Holland (2011), Influence of initial conditions and climate forcing on predicting Arctic sea ice, *Geophys. Res. Lett.*, *38*, L18503, doi:10.1029/2011GL048807.

Cole, S. T., M. L. Timmermans, J. M. Toole, R. A. Krishfield, and F. T. Thwaites (2014), Ekman veering, internal waves, and turbulence observed under Arctic sea ice, *J. Phys. Oceanogr.*, *44*, 1306–1328.

Gill, A. (1982), *Atmosphere-Ocean Dynamics, Int. Geophys. Ser.*, vol. 30, Academic Press, San Diego, Calif.

Grumbine, R. (2013), Long range sea ice drift model verification, *MMAB Tech. Note 315*, Natl. Cent. for Environ. Predict., Washington, D. C.

Grumbine, R. W. (1998), Virtual floe ice drift forecast model intercomparison, *Weather Forecasting*, *13*, 886–890.

Hibler, W. D. (1979), A dynamic thermodynamic sea ice model, *J. Phys. Oceanogr.*, *9*(4), 815–846.

Hibler, W. D., III (1980), Modeling a variable thickness sea ice cover, *Mon. Weather Rev.*, *108*, 1943–1973.

Holland, D. M. (2000), Merged IBCAO/ETOPO5 Global Topographic Data Product, Natl. Geophys. Data Cent., Boulder, Colo. [Available at http://www.ngdc.noaa.gov/mgg/bathymetry/arctic/ibcaorelatedsites.html.]

Kalnay, E., et al. (1996), The NCEP/NCAR 40-year reanalysis project, *Bull. Am. Meteorol. Soc.*, *77*, 437–471.

Kreyscher, M., M. Harder, P. Lemke, and G. M. Flato (2000), Results of the sea ice model intercomparison project: Evaluation of sea ice rheology schemes for use in climate simulations, *J. Geophys. Res.*, *105*, 11,299–11,320.

Kwok, R., and N. Untersteiner (2011), New high-resolution images of summer Arctic sea ice, *Eos Trans. AGU*, *92*, 53–54.

Lindsay, R., M. Wensnahan, A. Schweiger, and J. Zhang (2014), Evaluation of Seven Different Atmospheric Reanalysis Products in the Arctic, *J. Clim.*, *27*(7), 2588–2606, doi:10.1175/Jcli-D-13-00014.1.

Lindsay, R. W., and J. Zhang (2006), Assimilation of ice concentration in an ice-ocean model, *J. Atmos. Oceanic Technol.*, *23*, 742–749.

Acknowledgments

We thank Wendy Ermold for providing IABP buoy data. Ron Lindsay and Bob *Grumbine* provided helpful suggestions and background material. Two reviewers are thanked for their thoughtful comments and suggestions. NCEP/NCAR Reanalysis data are provided by the NOAA Physical Sciences Division (http://www.esrl.noaa.gov/psd/data/reanalysis/reanalysis.shtml). CFS data were obtained from (http://cfs.ncep.noaa.gov/). This research was supported by grants from the Office of Naval Research, the National Science Foundation Polar Programs, and the NASA Cryosphere Program.

Liu, Z., A. Schweiger, and R. Lindsay (2014), Observations and modeling of atmospheric profiles in the Arctic seasonal ice zone, *Mon. Weather Rev.*, *143*, 39–53.
Manda, A., N. Hirose, and T. Yanagi (2005), Feasible method for the assimilation of satellite-derived SST with an ocean circulation model, *J. Atmos. Oceanic Technol.*, *22*, 746–756, doi:10.1175/JTECH1744.1.
Marchuk, G. I., and B. A. Kagan (1989), *Dynamics of Ocean Tides*, 327 pp., Kluwer Acad., Dordrecht, Boston.
Olason, E., and D. Notz (2014), Drivers of variability in Arctic sea-ice drift speed, *J. Geophys. Res. Oceans*, *119*, 5755–5775, doi:10.1002/2014JC009897.
Parkinson, C. L., and W. M. Washington (1979), Large-scale numerical-model of sea ice, *J. Geophys. Res.*, *84*, 311–337.
Peralta-Ferriz, C., and R. A. Woodgate (2015), Seasonal and interannual variability of pan-Arctic surface mixed layer properties from 1979 to 2012 from hydrographic data, and the dominance of stratification for multiyear mixed layer depth shoaling, *Prog. Oceanogr.*, *134*, 19–53.
Persson, P. O. G. (2011), Relative roles of wind forcing and ice dynamics for predicting short-term sea-ice movement as estimated from in-situ observations, paper presented at World Climate Research Programme Open Science Conference, World Clim. Res. Programme, Denver, 24–28 Oct.
Persson, P. O. G., C. W. Fairall, E. L. Andreas, P. S. Guest, and D. K. Perovich (2002), Measurements near the Atmospheric Surface Flux Group tower at SHEBA: Near-surface conditions and surface energy budget, *J. Geophys. Res.*, *107*(C10), 8045, doi:10.1029/2000JC000705.
Posey, P. G., et al. (2015), Improving Arctic sea ice edge forecasts by assimilating high horizontal resolution sea ice concentration data into the US Navy's ice forecast systems, *Cryosphere*, *9*, 1735–1745, doi:10.5194/tc-9-1735-2015.
Preller, R. H., and P. G. Posey (1989), The polar ice prediction system—A sea ice forecasting system, *NORDA Rep. 212, Code PDW 106-08*, 45 pp., Naval Ocean Research and Development Activity, Stennis Space Center, Miss.
Rampal, P., J. Weiss, and D. Marsan (2009), Positive trend in the mean speed and deformation rate of Arctic sea ice, 1979-2007, *J. Geophys. Res.*, *114*, C05013, doi:10.1029/2008JC005066.
Rigor, I. G., R. L. Colony, and S. Martin (2000), Variations in surface air temperature observations in the Arctic, 1979-97, *J. Clim.*, *13*, 896–914.
Saha, S., et al. (2010), The NCEP climate forecast system reanalysis, *Bull. Am. Meteorol. Soc.*, *91*, 1015–1057.
Saha, S., et al. (2014), The NCEP climate forecast system version 2, *J. Clim.*, *27*, 2185–2208.
Schweiger, A., R. W. Lindsay, J. Zhang, M. Steele, H. Stern, and R. Kwok (2011), Uncertainty in modeled Arctic sea ice volume, *J. Geophys. Res.*, *116*, C00D06, doi:10.1029/2011JC007084.
Smith, R., J. Dukowicz, and R. Malone (1992), Parallel ocean general circulation modeling, *Physica D*, *60*(1–4), 38–61.
Stroeve, J., L. C. Hamilton, C. M. Bitz, and E. Blanchard-Wrigglesworth (2014a), Predicting September sea ice: Ensemble skill of the SEARCH Sea Ice Outlook 2008-2013, *Geophys. Res. Lett.*, *41*, 2411–2418, doi:10.1002/2014GL059388.
Thomas, D. (1999), The quality of sea ice velocity estimates, *J. Geophys. Res.*, *104*, 13,627–13,652.
Thorndike, A. S., and R. Colony (1982), Sea ice motion in response to geostrophic winds, *J. Geophys. Res.*, *87*, 5845–5852.
Zhang, J. (2005), Warming of the arctic ice-ocean system is faster than the global average since the 1960s, *Geophys. Res. Lett.*, *32*, L19602, doi:10.1029/2005GL024216.
Zhang, J., and D. A. Rothrock (2001), A thickness and enthalpy distribution sea-ice model, *J. Phys. Oceanogr.*, *31*, 2986–3001.
Zhang, J., and D. A. Rothrock (2003), Modeling global sea ice with a thickness and enthalpy distribution model in generalized curvilinear coordinates, *Mon. Weather Rev.*, *131*, 681–697.
Zhang, J., and M. Steele (2007), The effect of vertical mixing on the Atlantic water layer circulation in the Arctic Ocean, *J. Geophys. Res.*, *112*, C04S04, doi:10.1029/2006JC003732.
Zhang, J., M. Steele, R. W. Lindsay, A. Schweiger, and J. Morison (2008a), Ensemble one-year predictions of arctic sea ice for the spring and summer of 2008, *Geophys. Res. Lett.*, *35*, L08502, doi:10.1029/2008GL033244.
Zhang, J., R. W. Lindsay, M. Steele, and A. Schweiger (2008b), What drove the dramatic retreat of Arctic sea ice during summer 2007?, *Geophys. Res. Lett.*, *35*, L11505, doi:10.1029/2008GL034005.
Zhang, J., R. Woodgate, and R. Moritz (2010), Sea ice response to atmospheric and oceanic forcing in the Bering Sea, *J. Phys. Oceanogr.*, *40*, 1729–1747, doi:10.1175/2010JPO4323.1.
Zhang, J., A. Schweiger, M. Steele, and H. Stern (2015a), Sea ice floe size distribution in the marginal ice zone: Theory and numerical experiments, *J. Geophys. Res. Oceans*, *120*, 3484–3498, doi:10.1002/2015JC010770.
Zhang, J., C. Ashjian, R. Campbell, Y. H. Spitz, M. Steele, and V. Hill (2015b), The influence of sea ice and snow cover and nutrient availability on the formation of massive under-ice phytoplankton blooms in the Chukchi Sea, *Deep Sea Res., Part II*, *118*, 122–135.
Zhang, J. L., R. Lindsay, A. Schweiger, and I. Rigor (2012), Recent changes in the dynamic properties of declining Arctic sea ice: A model study, *Geophys. Res. Lett.*, *39*, L20503, doi:10.1029/2012GL053545.